Infrared plasmonics: STEM-EELS characterization of Fabry-Pérot resonance damping in gold nanowires

Yueying Wu,[1,2,*] Zhongwei Hu,[3,*] Xiang-Tian Kong,[3] Juan Carlos Idrobo,[4] Austin G. Nixon,[3]
Philip D. Rack,[2,4] David J. Masiello,[3,†] and Jon P. Camden[1,‡]

[1]*Department of Chemistry and Biochemistry, University of Notre Dame, Notre Dame, Indiana 46556, USA*
[2]*Department of Materials Science and Engineering, University of Tennessee, Knoxville, Tennessee 37996, USA*
[3]*Department of Chemistry, University of Washington, Seattle, Washington 98195, USA*
[4]*Center for Nanophase Materials Sciences, Oak Ridge National Laboratory, Oak Ridge, Tennessee 37831, USA*

Materials possessing strong midinfrared responses are of current interest because of their potential application to long-wavelength metamaterials, photonic devices, molecular detection, and catalysis. Here, we utilize high-energy resolution (80 cm^{-1}, 10 meV) electron-energy-loss spectroscopy (EELS) in a monochromated and aberration-corrected scanning transmission electron microscope (STEM) to resolve multipolar surface plasmon resonances (SPRs), sometimes called Fabry-Pérot (FP) resonances, in gold nanowires with mode energies spanning from ∼1000 to 8000 cm^{-1}. STEM-EELS provides access to these mid- to near-IR responses in a single acquisition, avoiding the difficulties inherent in obtaining the same data using near-field optical techniques. The experimentally measured FP resonance energies and linewidths, together with analytical modeling and full-wave numerical electrodynamics simulations, provide a comprehensive picture of the radiative and intrinsic contributions to the total damping rates. We find some FP modes with dephasing times >60 fs, which is almost twice the longest previously reported plasmon dephasing time for individual Au nanoparticles in the infrared. The long dephasing times and the broad tunability of the FP resonance energies throughout the infrared region suggest additional opportunities for harnessing infrared plasmonic energy before dephasing occurs.

I. INTRODUCTION

Surface plasmon resonances (SPRs) in noble metal nanostructures have been intensively studied [1–3] in the visible and near-infrared (near-IR) parts of the spectrum [4,5], however, the midinfrared (mid-IR) spanning 320–3300 cm^{-1} (40–410 meV) is far less explored [6]. The latter regime is particularly interesting because it encompasses the excitations in phononic materials [7–9], as well as the vibrational fingerprint region of small molecules, biomolecules, and polymers [10,11]. Investigating IR plasmons, therefore, has fundamental relevance for developing new infrared metamaterials [6], for realizing the ultrasensitive and label-free detection of molecules [12,13], and for selectively driving the vibrations in surface-bound molecules [11,14,15].

Mid- and far-IR plasmons are most often probed by far-field optical microscopies [16–23], which are spatially and spectrally limited by diffraction and by selection rules, respectively. While scanning near-field optical microscopy (SNOM) expands the scope of optical interrogation, the available light sources are limited in the mid- and far-IR and analysis of the data is complicated by convolution of the tip and sample [24,25]. In contrast to optical methods, electron-energy-loss

spectroscopy (EELS) in a scanning transmission electron microscope (STEM) is capable of exciting all SPR modes in a nanostructure and has the advantage of superior (<1 nm) spatial resolution. Until very recently, EELS studies of SPRs were restricted to the near-IR and visible spectral windows, due to insufficient energy resolution in STEM-EELS [5]. The development of high-resolution EELS (≲20 meV) in recent years [26,27], however, has opened access to the characterization of mid-IR SPRs and provides a window into plasmon lifetimes. STEM/EELS further has the ability to probe, in one spectral acquisition, an energy range that would be difficult to cover with the corresponding optical experiments. Plasmon lifetimes are of special importance because they encode the underlying energy dissipation mechanisms resulting from radiative and nonradiative damping as well as control how a nanoparticle couples with its local environment.

In this paper, we utilize the high-energy resolution (80 cm^{-1}; 10 meV) EELS of Oak Ridge National Laboratory's monochromated aberration-corrected (MAC)-STEM [28,29] to resolve multipolar SPRs in Au nanowires with mode energies spanning from ∼1000 to 8000 cm^{-1} (∼120 to 990 meV). In addition to reporting the resonance energy as a function of the mode number and nanowire length, we examine in detail how different damping mechanisms are influenced by the resonance energy and mode structure of each SPR. The experimental observations are interpreted via analytical modeling and numerical electrodynamics simulation of the STEM electron probe [30,31]. Our results show that

*These authors contributed equally to this work.
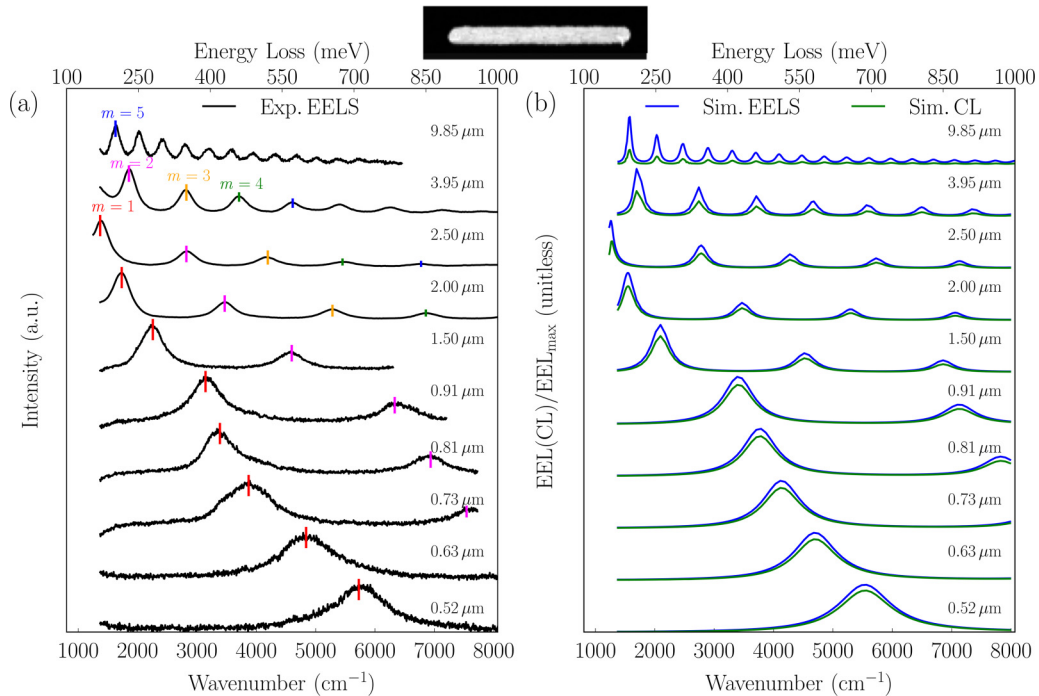†masiello@uw.edu
‡jon.camden@nd.edu

FIG. 1. Comparison of experimentally measured (left) and simulated EEL spectra (right) of Au nanowires. (a) STEM-EELS spectra of Au nanowires with lengths ranging from 0.52 to 9.8 μm. The spectra were acquired with an electron probe impact parameter of 10 nm outside the nanowire, along the long axis. The FP modes up to order $m = 5$ are indicated by a colored vertical bar. (b) Simulated EEL and CL spectra of the same nanowires obtained at the same impact parameter.

the plasmon lifetimes can decrease well below the quasistatic (Drude) limit, suggesting other ways to harness plasmonic energy before dephasing occurs.

II. RESULTS AND DISCUSSION

Au nanowires support multipolar SPR resonances spanning from the visible to mid-IR that can be progressively tuned by changing the nanowire aspect ratio, making them ideal for this study. We focus specifically on the nanowire's so-called Fabry-Pérot (FP) resonances, which result from the interference of two counterpropagating surface plasmon polaritons (SPPs) within a nanowire [32]. The interference condition leads to multiple resonant modes satisfying $kL = m\pi - \Phi$, where k is the SPP wave vector, $m = 1, 2, 3, \ldots$ is the mode number, L is the length of the nanowire, and Φ is the phase shift of the SPP wave upon reflection at the nanowire ends [32–34]. These modes alternate in parity (i.e., even, odd), nonetheless, the electrons in the STEM are capable of probing all nanowire responses independent of parity. Although previous STEM-EELS studies address dispersion of guided SPPs [35], plasmon-induced near-field distributions [33,36–43], SPP propagation length [41,44], nanowire coupling [45], and plasmon damping [46] in the visible, a detailed study of the plasmon dephasing times in individual nanostructures in the infrared still needs to be presented. In this paper, we utilize the high spectral resolution now available in monochromated STEMs to study the contribution of different decay channels to the plasmon damping and linewidth in the mid-IR as a function of both nanowire length and mode structure.

Figure 1(a) presents experimental EEL spectra obtained from ten nanowires of varying length (0.5–10 μm) acquired by placing the electron probe near the nanowire tip at an impact parameter of 10 nm (see the Appendix). To aid in the interpretation of the data, numerical EELS and cathodoluminescence (CL) simulations of the nanowire spectra are plotted in Fig. 1(b).

In general, a progressive redshift of the FP modes is observed as L increases. The dipole ($m = 1$) and higher-order modes shift into the mid-IR and eventually start to partially overlap, as seen in the 9.8-μm nanowire. We are able to observe the $m = 1$ mode in the EEL spectra of all nanowires with $L < 2.5$ μm, while the first identifiable mode for the 3.95- and 9.8-μm nanowire is $m = 2$ and $m = 5$, respectively. The simulations agree well with experiments and aid the identification of mode order in the longest nanowires ($L > 2.5$ μm); see Supplemental Material Fig. S1 [47]. The experiments also show that the FP resonance linewidths progressively narrow with increasing L, a trend that is also observed in the simulated EEL and CL spectra. The experimental linewidths are in general slightly larger than those in simulations; however, this is attributed to the additional damping induced with grain boundaries, surface roughness, and imperfections in the lithographic Au nanowires, and substrate effects.

The resonance energies of the individual nanowire FP modes are summarized in Fig. 2. While the resonance energies of the first five FP modes ($m = 1$–5) do not depend linearly upon L, the energy gap between two consecutive modes in each nanowire is consistent within a given nanowire length, $\Delta E_{gap} = E_{m+1} - E_m$, where E_m is the mth FP resonance energy. When plotted as a function of the nanowire
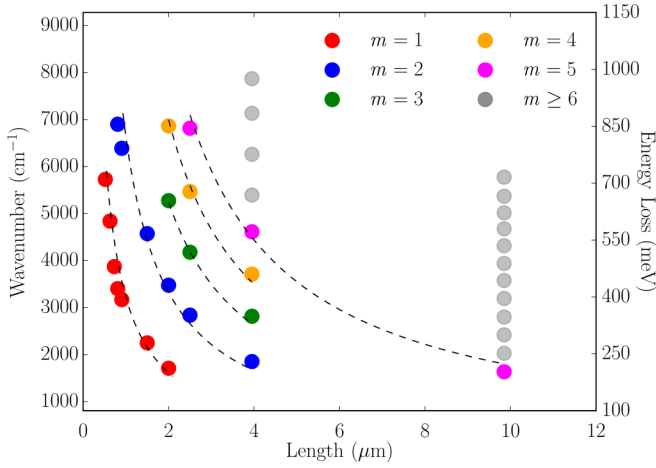
FIG. 2. Experimentally measured FP resonance energies as a function of Au nanowire length. m indicates the order of the FP mode. The dashed black lines are added only to guide the eye.

length, the average energy gap between modes follows a power law, $\Delta \bar{E}_{gap} = 380$ meV $(1\ \mu m/L)^{0.9}$; see Supplemental Material Fig. S3 [47]. This tunable energy gap between modes may be useful for different applications such as plasmon bandpass filters, manipulating energy transfer, or selectively detecting/interacting with different surface molecules.

Trends in both the mode energy and linewidth can be elucidated using a theoretical analysis of the FP resonance energy and linewidth based on a general form of the nanowire spectrum in EELS. In particular, the EEL FP line shape stems from the imaginary part of the Lorentzian polarizability,

$$\alpha_m(\omega) = \frac{\alpha_0 \omega_m^2}{\omega_m^2 - i\gamma_m \omega - \omega^2}, \quad (1)$$

where α_0, ω_m, and γ_m are the high-frequency-limit polarizability, the resonant frequency, and the frequency-dependent damping rate of the mth FP mode. The latter includes both radiative and nonradiative dissipation processes. On resonance, i.e., $\omega = \omega_m$, the magnitude of the polarizability is $\alpha_m^{max} = i\alpha_0 \omega_m/\gamma_m$. Thus, as the damping rate decreases, the imaginary part of the polarizability increases and so too does the amplitude of the mth FP resonance in the EEL spectrum, which is proportional to Im$[\alpha_m(\omega)]$.

The optical response of a prolate spheroid provides a useful qualitative model for the FP resonance energy and linewidth of the Au nanowires studied here. When considering the $m = 1$ mode of the nanowire, Eq. (1) can be explicitly derived from the polarizability of a prolate spheroid, including the dependence of its parameters upon the spheroid geometry, material composition, and retardation effects (see Supplemental Material [47]) [48–51]. The fully retarded approach taken here is important because the contribution of the dynamic polarization and radiation reaction to the polarizability becomes prominent for long nanowires.

Using a Drude free-electron gas model of Au, i.e., $\varepsilon(\omega) = \varepsilon_\infty - \omega_p^2/\omega(\omega + i\gamma_D)$, with ε_∞, ω_p, and γ_D being the high-frequency dielectric constant, plasma frequency, and nonradiative damping rate, together with the approximations $\varepsilon_\infty \ll$ Re(ε) and $(\varepsilon_\infty - \varepsilon_b)/\varepsilon \sim 0$, which are appropriate for IR dipole resonances, the dipolar parameters of the Lorentzian

polarizability in Eq. (1) take on the explicit forms,

$$\alpha_0 = \frac{V}{4\pi l}, \quad \omega_1^2 = \frac{l\omega_p^2}{n_b^2}\beta, \quad \gamma_1 = \gamma_1'\beta. \quad (2)$$

Here, ε_b and $n_b = \varepsilon_b^{1/2}$ are the permittivity and refractive index of the background medium, V is the spheroid volume, $\gamma_1' = \gamma_D + (V/6\pi)\omega_p^2 n_b(\omega^2/c^3)$, and $\beta = 4\pi l_E c^2/(4\pi l_E c^2 + VD\omega_p^2)$. The definitions of the geometrical parameters l, D and l_E are provided in Supplemental Material [47] (see also Refs. [49,50]). Equation (2) shows that both the resonance frequency (ω_1) and damping rate (γ_1) are related to the scaling factor β, which is less than one for the longitudinal dipole mode and decreases with increasing aspect ratio. As a result, the full width at half maximum (FWHM) of the dipolar extinction spectrum,

$$\hbar \Gamma_1 = \hbar \gamma_1(\omega_1) = \hbar \left(\gamma_D + \frac{V}{6\pi} \frac{l\omega_p^4}{n_b c^3}\beta \right)\beta, \quad (3)$$

also decreases with increasing aspect ratio and, interestingly, can even lie below the bulk Drude damping contribution ($\hbar\gamma_D$) for very long nanowires.

Figure 3(a) shows a comparison of the experimentally measured, analytically calculated, and full-wave electrodynamics simulated dispersion of the dipolar FP mode. As both optical extinction and EELS are proportional to Im$[\alpha_m(\omega)]$ [52], the calculated extinction coefficient $C_{ext} = \sigma_{ext}/\sigma_{geo}$ is displayed using a the red color scale (σ_{ext} and σ_{geo} being the extinction cross section and geometric cross section). The experimental and simulated resonance energies are overlaid as the green and purple dots, respectively. As the FP resonance moves to lower energies, the dispersion of the mode becomes close to the light line in air (shown as the dotted line). The mode becomes less confined to the metal domain and its resonance energy and damping rate are significantly affected by the dynamic polarization and radiation reaction processes. As a consequence, the dipolar FP mode ($m = 1$) is strongly redshifted compared with the quasistatic limit case (dashed line). Figure 3(b) shows the evolution of the FWHM with increasing nanowire length L, as well as the crossover where $\hbar \Gamma_1$ becomes smaller than $\hbar\gamma_D$. This behavior occurs as the dipole mode energy decreases and the screening effect of the metal becomes increasingly strong. In this low-energy and large-size regime, most of the energy carried by the FP mode is expelled from the lossy metal volume into the surrounding dielectric medium, resulting in a decreased damping frequency and an increased polarizability.

To further elucidate the dependence of the dipolar FP mode's spatial field profile upon the aspect ratio, Fig. 4(a) illustrates the dipolar electric potential and field induced in a prolate spheroid by a uniform z-polarized field described by $\Phi_0 = -E_0 z$. Figures 4(b) and 4(c) show the internal and external field profiles corresponding to a progression of gold spheroids spanning from $b = (0.52$–$9.85)/2\ \mu m$ in the major axis length, all with a common minor axis length of $a = 32$ nm. It is evident that the constant field induced inside the spheroid progressively decreases while the external induced field extends further into the surrounding dielectric medium (taken to be vacuum) as the spheroid aspect ratio (b/a) increases. In the dipole limit, the induced potential
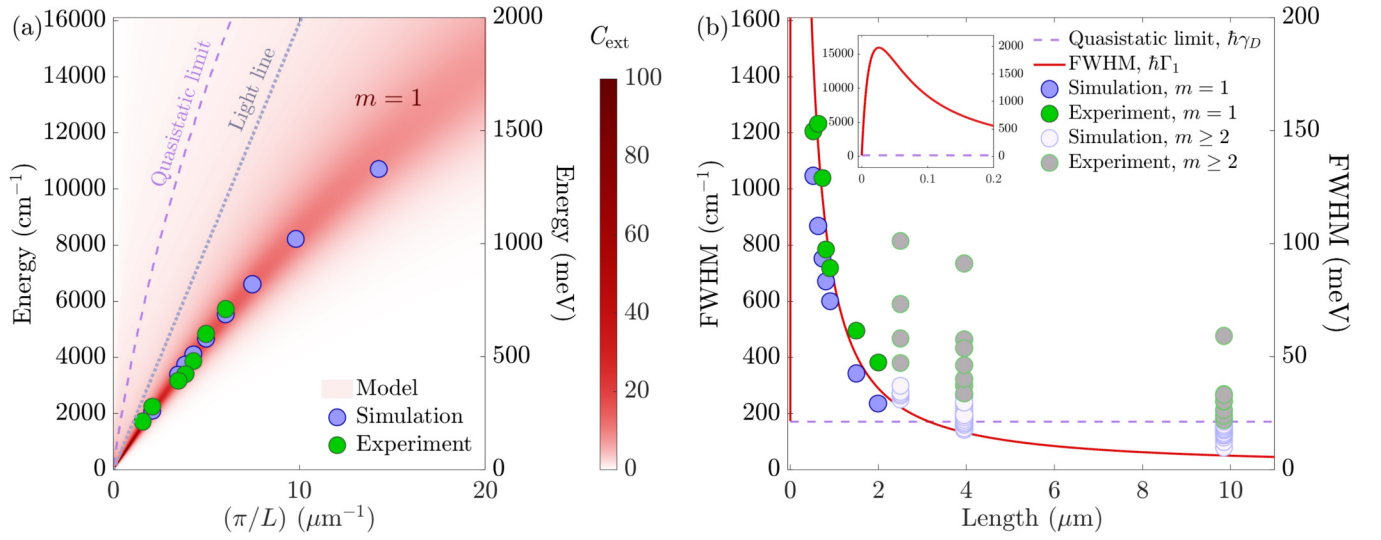
FIG. 3. Comparison of experimental, theoretical, and simulated FP dispersion curves, mode energies, and mode linewidths. (a) Dispersion curve for dipolar ($m = 1$) FP mode. The red shading denotes the extinction coefficient of the dipolar FP mode calculated from the analytic model. The experimental (green dots) and simulated (purple dots) track well with the analytical extinction coefficient. The vacuum light and quasistatic dipolar mode dispersion curves are shown for comparison. (b) Experimental and simulated FWHMs for all FP modes obtained from the EEL spectra in Fig. 1 as a function of nanowire length. The experimental (solid green) and simulated (solid purple) FWHMs for the dipolar ($m = 1$) FP modes are compared to the FWHM obtained from the analytical model. The FWHM decreases as L increases, with the analytic value eventually falling below the Drude linewidth (dashed line) near $L = 2.5\,\mu m$. The FWHMs of higher-order FP modes ($m > 1$, gray dots) are presented for comparison. The inset shows the FWHM behavior for small nanowire lengths.
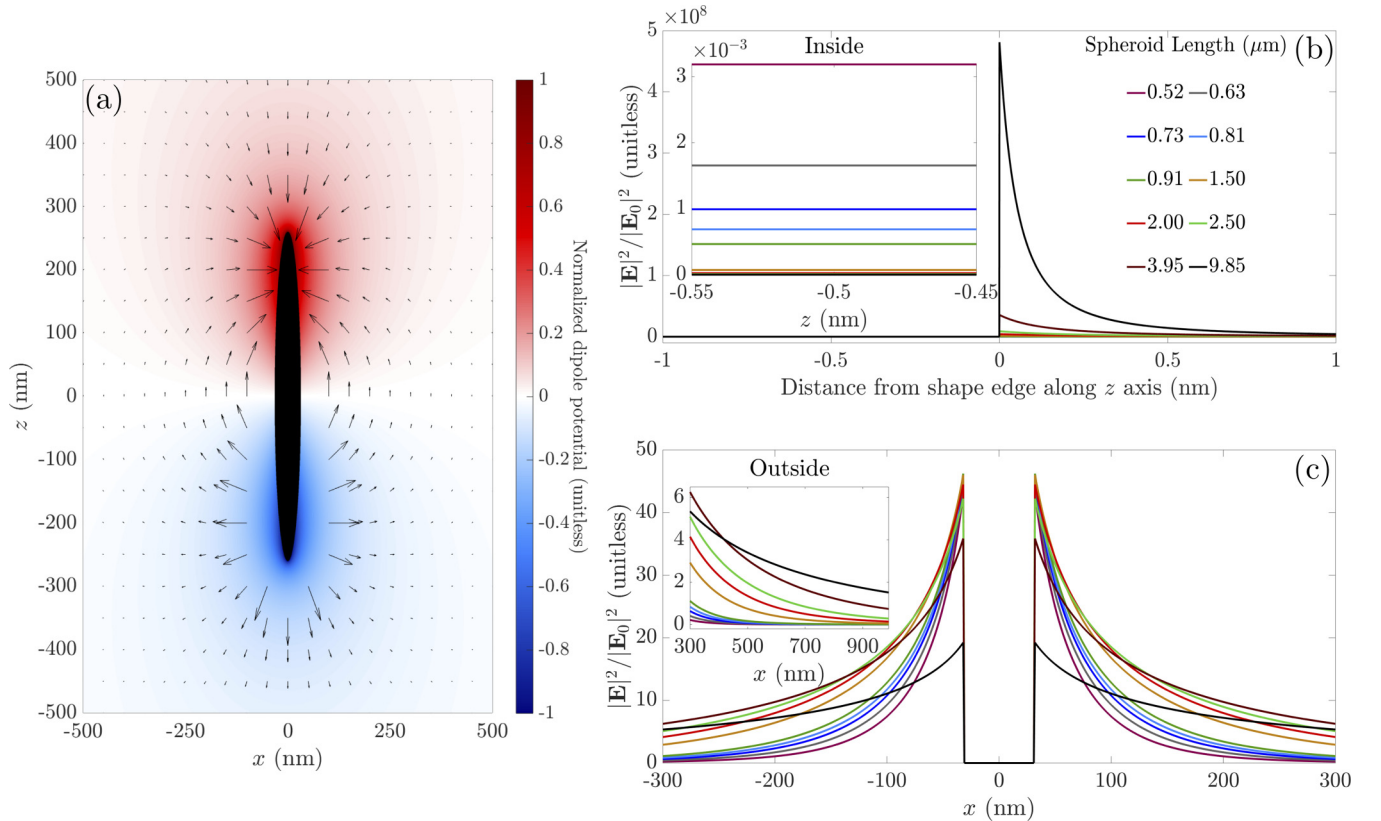

FIG. 4. Induced potential and electric field of a gold prolate spheroid placed in a uniform z-polarized field (a). Evolution of the induced electric field along the applied field polarization axis $(0, 0, z)$ (b) and perpendicular to the applied field polarization axis $(x, 0, 0)$ (c), clearly showing the increasing spill-out and decreasing internal magnitude of the induced field with increasing spheroid aspect ratio.
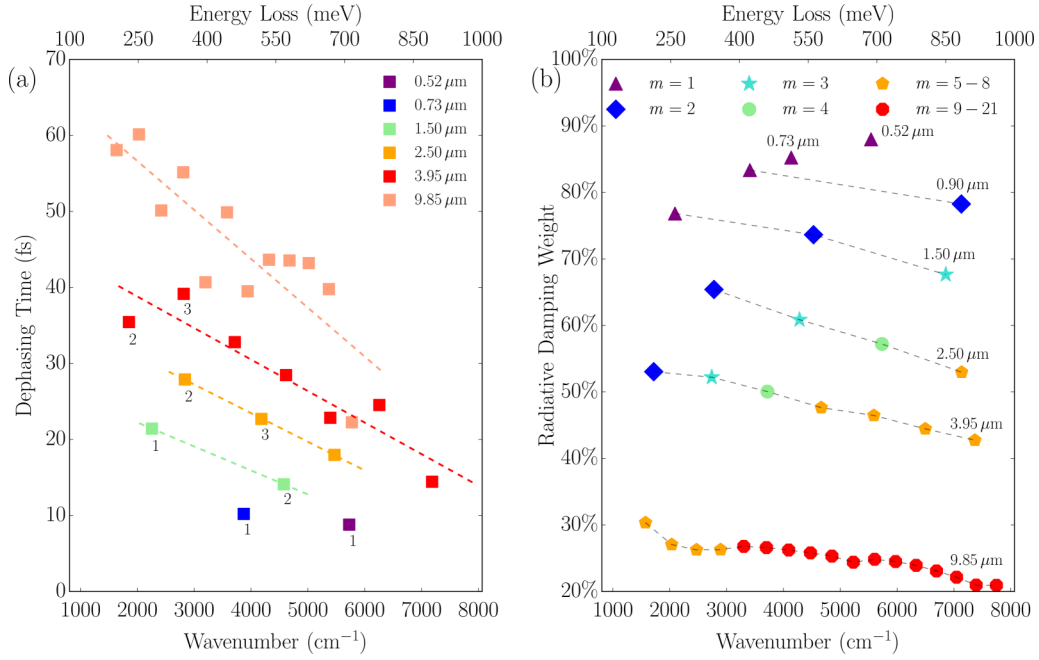
FIG. 5. (a) Experimental plasmon dephasing times for Au nanowires of selected lengths. The dashed lines are provided to guide the eye. The first three FP modes are labeled according to $m = 1, 2, 3$. (b) Radiative damping weights determined from the intensity ratio of the simulated CL/EEL spectra shown in Fig. 1. Data from the same nanowire are connected by dashed lines to guide the eye.

$$\Phi_{\text{ind}}^{\text{out}}(\xi, \eta, \phi) = AE_0 z(\coth^{-1}\xi - \xi^{-1})$$ and field

$$\frac{\mathbf{E}_{\text{ind}}^{\text{out}}(\xi, \eta, \phi)}{E_0} = -A\sqrt{\frac{\xi^2 - 1}{\xi^2 - \eta^2}}\eta\left(\coth^{-1}\xi - \frac{\xi}{\xi^2 - 1}\right)\hat{\boldsymbol{\xi}}$$
$$-A\sqrt{\frac{1 - \eta^2}{\xi^2 - \eta^2}}(\xi\coth^{-1}\xi - 1)\hat{\boldsymbol{\eta}} \qquad (4)$$

outside and inside

$$\frac{\mathbf{E}_{\text{ind}}^{\text{in}}(\xi, \eta, \phi)}{E_0} = -A(\tanh^{-1}e - e^{-1})\hat{\mathbf{z}} \qquad (5)$$

the spheroid are determined by solving Laplace's equations in prolate spheroidal coordinates [53], with focus $f = \sqrt{b^2 - a^2}$, eccentricity $e = f/b$, and dipole amplitude $A = \alpha_1(\omega)/(f^2 b/3)$ [see Eq. (1) and Supplemental Material Eq. (S1) [47]]. A connection between these curvilinear coordinates and Cartesian coordinates can be made through

$$\xi(x, y, z) = [\sqrt{x^2 + y^2 + (z + f)^2} + \sqrt{x^2 + y^2 + (z - f)^2}]/2f,$$
$$\eta(x, y, z) = [\sqrt{x^2 + y^2 + (z + f)^2} - \sqrt{x^2 + y^2 + (z - f)^2}]/2f,$$
$$z = f\xi\eta$$

with unit vectors

$$\hat{\boldsymbol{\xi}} = \sqrt{(1 - \eta^2)/(\xi^2 - \eta^2)}\xi(\cos\phi\hat{\mathbf{x}} + \sin\phi\hat{\mathbf{y}})$$
$$+ \sqrt{(\xi^2 - 1)/(\xi^2 - \eta^2)}\eta\hat{\mathbf{z}},$$
$$\hat{\boldsymbol{\eta}} = -\sqrt{(\xi^2 - 1)/(\xi^2 - \eta^2)}\eta(\cos\phi\hat{\mathbf{x}} + \sin\phi\hat{\mathbf{y}})$$
$$+ \sqrt{(1 - \eta^2)/(\xi^2 - \eta^2)}\xi\hat{\mathbf{z}}$$
$$\hat{\boldsymbol{\phi}} = -\sin\phi\hat{\mathbf{x}} + \cos\phi\hat{\mathbf{y}}.$$

This process additionally applies to the higher-order modes, i.e., $m \geqslant 2$. The experimental linewidths of the dipole and higher-order modes are shown in Fig. 3(b). While the dipole mode of the $L > 2.5\,\mu$m nanowires shifts out of the experimental detection window, the simulations show that the higher-order modes approach the quasistatic limit for the 3.95- and 9.85-μm Au wires. This behavior indicates a prolonged plasmon lifetime as the resonance energy is redshifted into the IR. We now turn to the dephasing times of the higher-order modes obtained from the experimental FWHM.

The dephasing time of the FP resonance depends on both the mode energy and the nanowire length. For any given SPR mode, the resonance energy decays (1) intrinsically via electron collisions with electrons, phonons, defects, interfaces, and Landau damping that causes local heating and (2) radiatively by reemitting photons into the far field. A damped SPR in general follows a Lorentzian profile in the frequency domain. The FWHM of an SPR is directly related to its dephasing time t as $t = 2/\Gamma$, where $\hbar\Gamma$ is the FWHM. t is defined as the time taken for the resonance amplitude to decay to $1/e$ of its original value [20,46]. Based on this relationship, the SPR dephasing time of optically bright modes has been widely characterized using optical techniques [16–20]. Given that our EEL spectra are obtained from a primary electron beam with a finite-energy resolution, the Lorentzian FP mode profile should be convolved with the width of the zero-loss peak (ZLP). Approximating the ZLP by a Gaussian function, the resulting FP modes will be observed in the EEL spectra as Voigt profiles. The Lorentzian linewidth of each FP mode can then be extracted by fitting each FP peak with a Voigt function (see Supplemental Material for spectrum fitting [47]). Using this procedure, the experimental dephasing times t of selected nanowires are calculated from the extracted Lorentzian FWHMs and plotted in Fig. 5(a).

Figure 5(a) shows that the dephasing time decreases as the mode order (*m*) increases. The dephasing time of the FP resonances in long nanowires can exceed 60 fs when the mode energy approaches the mid-IR ($\sim$1500 cm^{-1}; $\sim$186 meV), about four times longer than that of localized surface plasmon resonances (LSPRs) in the visible range, which is on the order of 6–10 fs [54,55]. Interestingly, this lifetime value is almost twice the longest previously measured plasmon dephasing time of individual gold nanoparticles in the infrared ($\sim$35 fs) [21]. It is also significantly longer than the maximum predicted dephasing time achievable for individual Au nanoparticles in the quasistatic limit ($\sim$30 fs), where electron-electron scattering and the temperature-independent component of the electron-phonon scattering limits the plasmon dephasing [56]. Considering that a typical C-H stretching mode ($\sim$3100 cm^{-1}; $\sim$384 meV) has a period of $\sim$10 fs, the mid-IR nanowire plasmons can provide a relatively long timescale for energy coupling or plasmon-assisted chemical reactions. To understand the origin of the long lifetimes observed here, we now turn to a detailed discussion of the damping processes in infrared nanowires.

The experimental dephasing times for first three FP modes ($m = 1, 2, 3$) are displayed in Fig. 5(a), showing the dependence of dephasing time on both mode order and mode energy. In these three modes, the dephasing time increases when the mode energy redshifts. Meanwhile, at a fixed energy, the experiments indicate that higher-order modes have a longer lifetime due to less radiative damping. The relative contribution from radiation damping and intrinsic damping can be estimated from simulations of the cathodoluminescence (CL) and EEL spectra. CL is the electron-beam-induced emission of radiation from the target, here produced by the radiation damping of the nanowire FP modes. The intensity ratio of simulated CL to EEL therefore serves as an approximation of the radiative contribution to the total damping for each mode.

The radiative contribution to the total damping, obtained from the CL/EELS simulations, is plotted in Fig. 5(b). Similar to previous observations of optical-frequency plasmons in Ag nanowires [57], radiation damping decreases with increasing mode order for a given nanowire. Not surprisingly, the dipole mode has the strongest radiation damping. Turning to the intrinsic damping, we note that the transverse component of an SPP generated at a metal/dielectric interface will decay into both the metal and dielectric side. For a single interface, it is well understood that the SPP penetration depth into the metal decreases as the mode energy decreases. This causes more of the SPP to spill out into the dielectric [6]. Therefore, the SPP suffers less intrinsic damping inside the metal. While the field distribution of a nanowire is more complex it qualitatively follows a similar trend.

It is now clear that the very long dephasing times observed here arise from multiple effects. First, radiation damping is decreasing as the mode energy decreases, as expected because of the reduced density of electromagnetic states available. Second, the intrinsic damping also decreases as the mode energy decreases, despite the fact that the metal dielectric function is actually becoming more lossy at these energies. We note that this mechanism differs from other processes such as Fano interference [58] and diffractive coupling [59]

in nanoparticle arrays that display spectrally narrow features in their infrared optical spectra.

III. CONCLUSION

In summary, FP resonances in Au nanowires with mode energies spanning from 1000 to 8000 cm^{-1} ($\sim$150 to $\sim$1000 meV) are measured using recently developed advances in monochromated STEM. The resonances progressively redshift with increasing nanowire length from the near- to mid-IR and become increasingly spectrally narrow. The FP mode dephasing times are directly extracted from the experimental linewidths of the resonance peaks and analyzed along with their mode energy distribution. We find that the lifetimes increase and exceed $\sim$60 fs in long nanowires when the mode energy shifts to the mid-IR. The radiative and intrinsic contributions to the total damping rate are examined within the context of an analytic model of a representative prolate spheroid as well as with full-wave numerical EELS simulations to understand the underlying damping mechanisms in the IR. These experiments illustrate the large spectral range accessible with single-acquisition STEM-EELS and its distinct advantages over all-optical methods when probing infrared plasmons. Future advances in electron energy monochromation will push the onset of this spectral observation window to even lower energies, thereby offering deeper insight into vibrational responses and other collective phenomena. Taken together, the unique plasmonic responses of noble metal nanowires in the near- to mid-IR calls attention to their potential for a variety of future applications such as biosensing and plasmon-mediated chemical reaction control.

simulations were facilitated through the use of advanced computational, storage, and networking infrastructure provided by the Hyak supercomputer system at the University of Washington. Numerical simulations were performed using computational resources supported by the University of Tennessee and Oak Ridge National Laboratory Joint Institute for Computational Sciences [60].

APPENDIX

1. Nanowire synthesis and characterization

Ten Au nanowires of varying length ($L = 0.52$, 0.63, 0.73, 0.81, 0.91, 1.5, 2.0, 2.5, 3.95, and 9.8 μm), with fixed thickness (0.03 μm) and width (0.1 μm), were patterned on a 0.02-μm-thick SiO_2 TEM membrane using electron beam lithography. These dimensions were chosen such that the nanowires support FP resonances in the near- to far-IR.

EELS measurements were conducted using a monochromated aberration-corrected Nion monochromated aberration-corrected STEM [61]. The STEM was operated at 60 kV with a collection semiangle (β) of 15 mrad, and a convergence semiangle (α) of 20 mrad. All spectra are collected by placing the electron beam at an impact parameter of 10 nm from the nanowire's long axis. The energy resolution of the STEM, taken to be FWHM of the zero-loss peak (ZLP), is ~10 meV. Each EEL spectrum is normalized to the intensity of the ZLP and the substrate contribution to the nanowire spectrum is removed using a background spectrum collected from the SiO_2 substrate far away from the nanowires.

2. Numerical simulation

EELS simulations were carried out using the electron-driven discrete dipole approximation (e-DDA) package [30,31] that inherits the coupled/discrete dipole framework [62,63] while describing the exciting field of a swift electron. The e-DDA has been used to study many different nanostructures [64–70], and thus it serves as an ideal simulation tool for the long nanowires studied here. The dimensions of all simulated Au nanowires were determined based on their experimental counterparts. To achieve a better agreement between experiment and theory, a relatively high discretization level (2 nm dipole spacing) was adopted for all nanowires. The only exception is the 9.85-μm nanowire, where a lower discretization level (3 nm dipole spacing) was used for numerical efficiency. The substrate (SiO_2) was explicitly modeled on an equal footing as the gold nanowire, i.e., by a collection of discrete dipoles, in order to capture substrate-induced image effects. Considering the IR EELS signals measured by the electron microscope, we have adapted appropriate dielectric constants for gold [71] and SiO_2 [72] that extend to low enough energy. In addition to EELS simulations, the CL results were also obtained using e-DDA.

[1] P. Jain, X. Huang, I. El-Sayed, and M. El-Sayed, Plasmonics **2**, 107 (2007).

[2] W. Hou and S. B. Cronin, Adv. Funct. Mater. **23**, 1612 (2013).

[3] E. Ozbay, Science **311**, 189 (2006).

[4] E. Hutter and J. H. Fendler, Adv. Mater. **16**, 1685 (2004).

[5] Y. Wu, G. Li, and J. P. Camden, Chem. Rev. **118**, 2994 (2018).

[6] Y. Zhong, S. D. Malagari, T. Hamilton, and D. M. Wasserman, J. Nanophotonics **9**, 093791 (2015).

[7] G. Z. Mashanovich, M. M. Milošević, M. Nedeljkovic, N. Owens, B. Xiong, E. J. Teo, and Y. Hu, Opt. Express **19**, 7112 (2011).

[8] M. P. Fischer, A. Riede, K. Gallacher, J. Frigerio, G. Pellegrini, M. Ortolani, D. J. Paul, G. Isella, A. Leitenstorfer, P. Biagioni, and D. Brida, Light: Sci. Appl. **7**, 106 (2018).

[9] R. A. Soref, J. Schmidtchen, and K. Petermann, IEEE J. Quantum Electron. **27**, 1971 (1991).

[10] R. P. Eischens and W. A. Pliskin, The infrared spectra of adsorbed molecules, in *Advances in Catalysis*, edited by D. D. Eley, W. G. Frankenburg, V. I. Komarewsky, and P. B. Weisz (Academic, New York, 1958), Vol. 10, pp. 1–56.

[11] F. Neubrech and A. Pucci, IEEE J. Sel. Top. Quantum Electron. **19**, 4600809 (2013).

[12] F. Neubrech, C. Huck, K. Weber, A. Pucci, and H. Giessen, Chem. Rev. **117**, 5110 (2017).

[13] C. Huck, M. Tzschoppe, R. Semenyshyn, F. Neubrech, and A. Pucci, Phys. Rev. Applied **11**, 014036 (2019).

[14] A. Agrawal, A. Singh, S. Yazdi, A. Singh, G. K. Ong, K. Bustillo, R. W. Johns, E. Ringe, and D. J. Milliron, Nano Lett. **17**, 2611 (2017).

[15] A. Konečná, T. Neuman, J. Aizpurua, and R. Hillenbrand, ACS Nano **12**, 4775 (2018).

[16] S. Link and M. A. El-Sayed, J. Phys. Chem. B **103**, 8410 (1999).

[17] H. Hövel, S. Fritz, A. Hilger, U. Kreibig, and M. Vollmer, Phys. Rev. B **48**, 18178 (1993).

[18] H. Baida, P. Billaud, S. Marhaba, D. Christofilos, E. Cottancin, A. Crut, J. Lermé, P. Maioli, M. Pellarin, M. Broyer, N. Del Fatti, F. Vallée, A. Sánchez-Iglesias, I. Pastoriza-Santos, and L. M. Liz-Marzán, Nano Lett. **9**, 3463 (2009).

[19] K. Kolwas and A. Derkachova, J. Quant. Spectrosc. Radiat. Transfer **114**, 45 (2013).

[20] C. Sonnichsen, T. Franzl, T. Wilk, G. von Plessen, J. Feldmann, O. Wilson, and P. Mulvaney, Phys. Rev. Lett. **88**, 077402 (2002).

[21] K. Ueno, Q. Sun, M. Mino, T. Itoh, T. Oshikiri, and H. Misawa, Opt. Express **24**, 17728 (2016).

[22] L. Razzari, A. Toma, M. Shalaby, M. Clerici, R. P. Zaccaria, C. Liberale, S. Marras, I. A. I. Al-Naib, G. Das, F. De Angelis, M. Peccianti, A. Falqui, T. Ozaki, R. Morandotti, and E. Di Fabrizio, Opt. Express **19**, 26088 (2011).

[23] W. T. Hsieh, P. C. Wu, J. B. Khurgin, D. P. Tsai, N. Liu, and G. Sun, ACS Photonics **5**, 2541 (2018).

[24] R. C. Dunn, Chem. Rev. **99**, 2891 (1999).

[25] L. Novotny and S. J. Stranick, Annu. Rev. Phys. Chem. **57**, 303 (2006).

[26] K. March, L. Scarabelli, L. M. Liz-Marzán, T. Aoki, P. Rez, H. Cohen, P. A. Crozier, O. L. Krivanek, O. Stéphan, and M. Kociak, The highest characterization potentialities of sub-20 meV spatially resolved STEM-EELS, in *European*

Microscopy Congress 2016: Proceedings (Wiley-VCH, Weinheim, 2016).

[27] O. L. Krivanek, T. C. Lovejoy, N. Dellby, T. Aoki, R. W. Carpenter, P. Rez, E. Soignard, J. Zhu, P. E. Batson, M. J. Lagos, R. F. Egerton, and P. A. Crozier, Nature (London) **514**, 209 (2014).

[28] J. A. Hachtel, J. Huang, I. Popovs, S. Jansone-Popova, J. K. Keum, J. Jakowski, T. C. Lovejoy, N. Dellby, O. L. Krivanek, and J. C. Idrobo, Science **363**, 525 (2019).

[29] J. A. Hachtel, A. R. Lupini, and J. C. Idrobo, Sci. Rep. **8**, 5637 (2018).

[30] N. W. Bigelow, A. Vaschillo, V. Iberi, J. P. Camden, and D. J. Masiello, ACS Nano **6**, 7497 (2012).

[31] N. W. Bigelow, A. Vaschillo, J. P. Camden, and D. J. Masiello, ACS Nano **7**, 4511 (2013).

[32] D. Rossouw, M. Couillard, J. Vickery, E. Kumacheva, and G. A. Botton, Nano Lett. **11**, 1499 (2011).

[33] O. Nicoletti, M. Wubs, N. A. Mortensen, W. Sigle, P. A. van Aken, and P. A. Midgley, Opt. Express **19**, 15371 (2011).

[34] E. Cubukcu and F. Capasso, Appl. Phys. Lett. **95**, 201101 (2009).

[35] D. Rossouw and G. A. Botton, Phys. Rev. Lett. **110**, 066801 (2013).

[36] J. Martin, M. Kociak, Z. Mahfoud, J. Proust, D. Gérard, and J. Plain, Nano Lett. **14**, 5517 (2014).

[37] H. Saito and H. Kurata, Microscopy **63**, 155 (2013).

[38] M. N'Gom, J. Ringnalda, J. F. Mansfield, A. Agarwal, N. Kotov, N. J. Zaluzec, and T. B. Norris, Nano Lett. **8**, 3200 (2008).

[39] M. N'Gom, S. Li, G. Schatz, R. Erni, A. Agarwal, N. Kotov, and T. B. Norris, Phys. Rev. B **80**, 113411 (2009).

[40] S. Yazdi, J. R. Daniel, N. Large, G. C. Schatz, D. Boudreau, and E. Ringe, Nano Lett. **16**, 6939 (2016).

[41] E. J. R. Vesseur, R. de Waele, M. Kuttge, and A. Polman, Nano Lett. **7**, 2843 (2007).

[42] H. Ditlbacher, A. Hohenau, D. Wagner, U. Kreibig, M. Rogers, F. Hofer, F. R. Aussenegg, and J. R. Krenn, Phys. Rev. Lett. **95**, 257403 (2005).

[43] L. Douillard, F. Charra, Z. Korczak, R. Bachelot, S. Kostcheev, G. Lerondel, P.-M. Adam, and P. Royer, Nano Lett. **8**, 935 (2008).

[44] B. Wild, L. Cao, Y. Sun, B. P. Khanal, E. R. Zubarev, S. K. Gray, N. F. Scherer, and M. Pelton, ACS Nano **6**, 472 (2012).

[45] M.-W. Chu, V. Myroshnychenko, C. H. Chen, J.-P. Deng, C.-Y. Mou, and F. J. García de Abajo, Nano Lett. **9**, 399 (2009).

[46] M. Bosman, E. Ye, S. F. Tan, C. A. Nijhuis, J. K. W. Yang, R. Marty, A. Mlayah, A. Arbouet, C. Girard, and M.-Y. Han, Sci. Rep. **3**, 1312 (2013).

[47] See Supplemental Material at http://link.aps.org/supplemental/10.1103/PhysRevB.101.085409 for information on (I) simulated electromagnetic field maps for Au nanowires, (II) fitting of EEL spectra, (III) averaged energy gap between FP modes, and (IV) analytical model.

[48] A. Wokaun, J. P. Gordon, and P. F. Liao, Phys. Rev. Lett. **48**, 957 (1982).

[49] A. Moroz, J. Opt. Soc. Am. B **26**, 517 (2009).

[50] H. Y. Chung, P. T. Leung, and D. P. Tsai, J. Chem. Phys. **131**, 124122 (2009).

[51] J. Gersten and A. Nitzan, J. Chem. Phys. **75**, 1139 (1981).

[52] A. Polman, M. Kociak, and F. J. García de Abajo, Nat. Mater. **18**, 1158 (2019).

[53] W. R. Smythe, *Static and Dynamic Electricity* (McGraw-Hill, New York, 1950).

[54] T. Klar, M. Perner, S. Grosse, G. von Plessen, W. Spirkl, and J. Feldmann, Phys. Rev. Lett. **80**, 4249 (1998).

[55] M. Scharte, R. Porath, T. Ohms, M. Aeschlimann, B. Lamprecht, H. Ditlbacher, and F. R. Aussenegg, Proc. SPIE **4456**, 449533 (2001).

[56] J. Olson, S. Dominguez-Medina, A. Hoggard, L.-Y. Wang, W.-S. Chang, and S. Link, Chem. Soc. Rev. **44**, 40 (2015).

[57] A. Losquin and M. Kociak, ACS Photonics **2**, 1619 (2015).

[58] M. Qin, L. Wang, X. Zhai, D. Chen, and S. Xia, Nanoscale Res. Lett. **12**, 578 (2017).

[59] V. G. Kravets, A. V. Kabashin, W. L. Barnes, and A. N. Grigorenko, Chem. Rev. **118**, 5912 (2018).

[60] http://www.jics.tennessee.edu.

[61] O. L. Krivanek, T. C. Lovejoy, N. Dellby, and R. W. Carpenter, Microscopy **62**, 3 (2013).

[62] B. T. Draine and P. J. Flatau, J. Opt. Soc. Am. A **11**, 1491 (1994).

[63] E. M. Purcell and C. R. Pennypacker, Astrophys. J. **186**, 705 (1973).

[64] Q. Liu, S. C. Quillin, D. J. Masiello, and P. A. Crozier, Phys. Rev. B **99**, 165102 (2019).

[65] C. Cherqui, G. Li, J. A. Busche, S. C. Quillin, J. P. Camden, and D. J. Masiello, J. Phys. Chem. Lett. **9**, 504 (2018).

[66] Y. Wu, G. Li, C. Cherqui, N. W. Bigelow, N. Thakkar, D. J. Masiello, J. P. Camden, and P. D. Rack, ACS Photonics **3**, 130 (2016).

[67] G. Li, C. Cherqui, Y. Wu, N. W. Bigelow, P. D. Simmons, P. D. Rack, D. J. Masiello, and J. P. Camden, J. Phys. Chem. Lett. **6**, 2569 (2015).

[68] C. Cherqui, N. W. Bigelow, A. Vaschillo, H. Goldwyn, and D. J. Masiello, ACS Photonics **1**, 1013 (2014).

[69] V. Iberi, N. W. Bigelow, N. Mirsaleh-Kohan, S. Griffin, P. D. Simmons, B. S. Guiton, D. J. Masiello, and J. P. Camden, J. Phys. Chem. C **118**, 10254 (2014).

[70] G. Li, C. Cherqui, N. W. Bigelow, G. Duscher, P. J. Straney, J. E. Millstone, D. J. Masiello, and J. P. Camden, Nano Lett. **15**, 3465 (2015).

[71] R. L. Olmon, B. Slovick, T. W. Johnson, D. Shelton, S.-H. Oh, G. D. Boreman, and M. B. Raschke, Phys. Rev. B **86**, 235147 (2012).

[72] J. Kischkat, S. Peters, B. Gruska, M. Semtsiv, M. Chashnikova, M. Klinkmüller, O. Fedosenko, S. Machulik, A. Aleksandrova, G. Monastyrskyi, Y. Flores, and W. T. Masselink, Appl. Opt. **51**, 6789 (2012).